JOURNAL OF SPACECRAFT AND ROCKETS
Vol. 44, No. 1, January–February 2007

Orbit Determination Using the Geomagnetic Field Measurement via the Unscented Kalman Filter

Kyoung-Min Roh,* Sang-Young Park,† and Kyu-Hong Choi‡
Yonsei University, Seoul 120-749, Republic of Korea

DOI: 10.2514/1.23693

Orbit determination of spacecraft using only magnetometer measurements via the unscented Kalman filter (UKF) is presented. An algorithm was formulated by adopting the UKF and an adequate dynamic model developed for processing geomagnetic field measurements. The paper consists of the analysis of force and estimation models, the dependency of position accuracy on orbit type, and measurement errors, as well as a comparison of the UKF and the extended Kalman filter (EKF). Finally, the developed algorithm used actual magnetometer flight data from the Magnetic Field Satellite (MAGSAT). The results obtained from the MAGSAT data demonstrate that the achieved position error was approximately 2 km. The UKF performs similar to the EKF in position accuracy for a sampling interval of less than 20 s. In contrast, for a sampling interval of 40 s, the EKF yields lower position accuracy than the UKF. In particular, the decomposed position errors are not biased because the UKF is not affected by linearization of the measurement function. This improvement makes the magnetometer-based orbit determination method more robust and reliable as a real-time orbit determination system for small satellites that require moderate position accuracy, and also as a backup orbit determination system for large satellites.

Nomenclature

$\boldsymbol{a}_{\text{drag}}$	=	acceleration due to atmospheric drag, m/s^2
$\boldsymbol{a}_{\text{geo}}$	=	acceleration due to geopotential, m/s^2
$\boldsymbol{a}_{\text{SRP}}$	=	acceleration due to the solar radiation pressure, m/s^2
$\boldsymbol{a}_{\text{sun/moon}}$	=	acceleration due to the sun and moon's gravity, m/s^2
B_r, B_θ, B_ϕ	=	the Earth magnetic field vector components, nT
B^*	=	inverse of the ballistic coefficient, m^2/kg
e	=	eccentricity
$\boldsymbol{F}$	=	system function
h	=	measurement function
i	=	orbital inclination, deg
$\boldsymbol{K}$	=	Kalman gain matrix
$\boldsymbol{P}$	=	covariance matrix
$\boldsymbol{P}^a$	=	augmented covariance matrix
$\boldsymbol{R}$	=	measurement covariance matrix
r	=	radial distance from the Earth, m
$\boldsymbol{r}$	=	position vector in J2000, m
t	=	time, s
T_{orb}	=	orbital period
$\boldsymbol{v}$	=	velocity vector in J2000, m/s
$\boldsymbol{w}$	=	system noise vector
$W^{(m)}$, $W^{(c)}$	=	weight factors for the state (m) and covariance (c)
$\boldsymbol{x}$	=	state vector
$\boldsymbol{x}^a$	=	augmented state vector, or $[\boldsymbol{x}^T, \boldsymbol{w}^T]^T$
y	=	measurement, nT
$\tilde{y}$	=	observed measurement
α, β, κ, and λ	=	scaling parameters for the unscented Kalman filter
γ	=	measurement of sigma point
η	=	measurement noise, nT
θ	=	east longitude, rad
ν	=	true anomaly, deg
σ	=	uncertainty (1 standard deviation) in a parameter
σ_{pos}	=	estimated standard deviation of position error, or $\sqrt{\sigma_x^2 + \sigma_y^2 + \sigma_z^2}$
ϕ	=	colatitude from the North Pole, rad
$\boldsymbol{\chi}$	=	sigma points ($\boldsymbol{\chi}^x$, $\boldsymbol{\chi}^w$)
Ω	=	right ascension of ascending node, rad
ω	=	argument of perigee, rad

Received 6 March 2006; revision received 7 August 2006; accepted for publication 8 August 2006.

*Ph.D. Candidate, Astrodynamics & Control Laboratory, Department of Astronomy and Space science; romin@galaxy.yonsei.ac.kr.

†Professor, Astrodynamics & Control Laboratory, Department of Astronomy and Space science; spark@galaxy.yonsei.ac.kr (corresponding author). Senior Member AIAA.

‡Professor, Astrodynamics & Control Laboratory, Department of Astronomy and Space science. Senior Member AIAA.

I. Introduction

AUTONOMOUS orbit determination of spacecraft using magnetometers has been studied and verified using real-flight data in many previous works [1–5]. The magnetometer has been of particular interest, because the sensor data can be used for real-time orbit determination in an onboard computer without any intervention from a ground station or space system such as the Global Positioning System. Furthermore, the sensor's low cost and reliability and relevance for attitude determination make it an attractive choice for real-time orbit determination. However, in earlier researches, errors in determination of the spacecraft's position ranged from 8 to hundreds of kilometers when magnetometer data was used exclusively [1–5]. This coarse accuracy is an obstacle for more practical applications of the magnetometer-based orbit determination method and is considered to be caused mainly by the inaccuracy of the geomagnetic field model. Therefore, in the majority of previous literature, the dynamic model, i.e., the orbital motion of a spacecraft, was modeled with J2 perturbation and atmospheric drag, in addition to estimating the ballistic coefficient, with the method for position estimation being used with the extended Kalman filter (EKF) [1–4]. Magnetometer-based orbit determination with the batch filter has also been studied. For example, Psiaki [6] used the batch filter with additional measurements from star sensor data, whereas Jung and Psiaki [7] added sun sensor data to magnetometer data and tuned the International Geomagnetic Reference Field (IGRF) model coefficients through the batch filter. Although these methods increased the position accuracy by approximately 3 km, this batch filter is not the proper method for real-

time orbit determination, because the measurement data used in the batch method should be collected for one or two days. Over the last few decades, with the help of enhancement in magnetometer technology and the success of the geomagnetic field exploration mission, the accuracy of the IGRF model has improved significantly from a standard error of several hundreds of nT in the 1960s to a few tens of nT in the 1980s [8]. This means that a more accurate position can be achieved by applying a suitable dynamic model and estimation method to the magnetometer.

The main purpose of the current study is to improve the real-time position accuracy of magnetometer-based orbit determination. To accomplish this goal, an algorithm has been formulated using the unscented Kalman filter (UKF) [9] and by selecting an appropriate dynamic model for geomagnetic field measurement. It is known the UKF performs well in nonlinear systems as the filter has been investigated widely in various applications, such as tracking a ballistic target [10] and estimating the attitude of a spacecraft [11,12]. Specifically, Lee and Alfriend [13–15] applied the UKF to orbit determination problems in successive studies and showed that the UKF is superior to the EKF in many respects such as overall accuracy, insensitivity to tuning parameters, and robustness to initial estimation errors. Cheon [5] also used the UKF to process geomagnetic field measurements for orbit determination although the results were based on a too-simplified dynamic model: two-body motion. In the current study, the performance of the UKF is compared with the results achieved by the EKF and is also applied to real-flight data of the Magnetic Field Satellite (MAGSAT). The orbit determination results are also analyzed on the basis of the effects of the dynamic model, orbit types, measurement errors, and linearization of measurement model.

II. Algorithm Formulation

The orbit determination algorithm is based on the predictor-corrector scheme, which is used generally for real-time orbit determination and consists of three parts: a system model (a dynamic model), a measurement model, and an estimation algorithm. The dynamic model is used to predict the state variables and their covariances. The measurement model allows to compute the modeled measurements and their partial derivatives with respect to the state variables. The "correction" process is carried out using the differences between the actual and predicted measurements. The prediction process in the UKF technique is different from that of the EKF, whereas the correction process was similar in the UKF and EKF techniques. A brief review of the UKF algorithm is included to provide insights into the orbit determination strategy of this paper, whereas the EKF algorithm is applied using the formulas contained in [16].

A. Dynamic Model

The dynamic model of satellite orbital motion for real-time applications should be defined carefully and take into consideration both computational efficiency and the accuracy of the measurement system. A precise dynamic model may be inadequate for a coarse measurement system, but could eventually increase the accuracy of the propagated orbital positions at the expense of heavy computational burden. Conversely, an excessively simplified dynamic model may degrade the performance of the filter regardless of computational efficiency. The orbital dynamic equations adopted in this work are

$$\dot{\boldsymbol{r}} = \boldsymbol{v} \tag{1}$$

$$\dot{\boldsymbol{v}} = \boldsymbol{a}_{\text{geo}} + \boldsymbol{a}_{\text{drag}} + \boldsymbol{a}_{\text{SRP}} + \boldsymbol{a}_{\text{sun/moon}} + \begin{bmatrix} w_1 \\ w_2 \\ w_3 \end{bmatrix} \tag{2}$$

$$\dot{B}^* = w_4 \tag{3}$$

where $\boldsymbol{r}$ and $\boldsymbol{v}$ are the position and velocity vectors in an inertial frame, and the coefficients w_{1-4} exhibit zero-mean white Gaussian noise. The coefficient B^* is the inverse of the ballistic coefficient of the satellite, defined by multiplication of the drag coefficient and the area-to-mass ratio, and is modeled as a random walk. The accelerations acting on the satellite, Eq. (2) consist of geopotential acceleration ($\boldsymbol{a}_{\text{geo(degree,order)}}$) and accelerations due to atmospheric drag, solar radiation pressure, and lunar and solar gravitational attractions. The JGM3 model for geopotential coefficients, the analytical formulas for the ephemeris of the sun and the moon, the constant solar radiation pressure, and the constant area-to-mass ratio from [17] are used in the system model. The atmospheric density of the system model is calculated using the Harris–Priester model [17]. In the current study, the five cases listed in Table 1, each with different state vectors and different levels of perturbations, have been tested to find an appropriate dynamic model for the system. The state vector of Case A, Case B, and Case C consists of the Cartesian position and velocity components in an inertial frame, whereas the state vector of Case D and Case E includes, in addition, the inverse of the ballistic coefficient.

Table 1 State vectors and accelerations of the dynamics models; number of subscript denotes degree and order of geopotential coefficients

Study case	State vector	Accelerations
A	$\begin{bmatrix} \boldsymbol{r}^T & \boldsymbol{v}^T \end{bmatrix}^T$	$\boldsymbol{a}_{\text{geo(20,20)}} + \boldsymbol{a}_{\text{drag}} + \boldsymbol{a}_{\text{SRP}} + \boldsymbol{a}_{\text{sun/moon}}$
B	$\begin{bmatrix} \boldsymbol{r}^T & \boldsymbol{v}^T \end{bmatrix}^T$	$\boldsymbol{a}_{\text{geo(2,0)}}$
C	$\begin{bmatrix} \boldsymbol{r}^T & \boldsymbol{v}^T \end{bmatrix}^T$	$\boldsymbol{a}_{\text{geo(4,4)}}$
D	$\begin{bmatrix} \boldsymbol{r}^T & \boldsymbol{v}^T & B^* \end{bmatrix}^T$	$\boldsymbol{a}_{\text{geo(2,0)}} + \boldsymbol{a}_{\text{drag}}$
E	$\begin{bmatrix} \boldsymbol{r}^T & \boldsymbol{v}^T & B^* \end{bmatrix}^T$	$\boldsymbol{a}_{\text{geo(4,4)}} + \boldsymbol{a}_{\text{drag}}$

The system process noise, which equates to the accuracy of the dynamic model, is applied only to the acceleration components and the ballistic coefficient to reduce the dimension of the augmented state vector. The process noises were predetermined by comparing the orbit generated by the dynamic model in this work with that from the high-precision orbit propagator (HPOP) in the satellite tool kit (STK) [18,19]. The orbit calculated from the HPOP is considered as a reference orbit in this study. The relative position and velocity errors with respect to the orbit from HPOP were calculated for a circular low-Earth-orbiting spacecraft. Their maximum velocity errors after 100-s propagation ranged from 0.0064 to 0.0077 m/s in all dynamic models except Case A (0.0007 m/s). Taking into account this propagation error, the standard variation of process noise (σ_{w1-w3}) in the acceleration components can be set from 1×10^{-4} to 1×10^{-5} m/s^2 in all the dynamic models referenced in this paper. The σ_{w4} was set to 0.04 m^2/kg/T_{orb}, where T_{orb} is the orbital period. For a low-Earth orbit, these variances were approximately 1×10^{-5} m^2/(kg · s) [1]. In the HPOP module, the Gauss–Jackson method for the numerical integration of the equations of motion, the EGM 96 model (up to a degree of 70 × 70) for perturbation due to the nonsymmetric geopotential, the Jacchia70 model for atmospheric density, and the DE403 JPL coefficient for the lunar/solar ephemeris were used in the HPOP. Atmospheric drag, lunar/solar gravitational attraction, and solar radiation pressure were also included. The atmospheric drag coefficient was set to 2.0, the solar radiation pressure coefficient set to 1.0, and the constant area-to-mass ratio set to 0.02 for use in the HPOP.

B. Measurement Model

Three-axis magnetometers are used generally for sensing the geomagnetic field. Each magnetometer is assumed to be aligned with the principal axis of a satellite. In the present study, only the scalar magnitude of the geomagnetic field measurements is used, so the estimation algorithm is independent of spacecraft attitude. There are two major error sources in the magnetometer-based orbit determination, i.e., the sensor error and the IGRF model error. These two errors are completely independent. For the sensor error, although biases may critically degrade position accuracy, these biases can be removed by estimating their value. However, the

inaccuracy of the IGRF model cannot be removed. The IGRF 2005 model [20] is used for the observed measurement simulations. The IGRF 2000 and IGRF 1980 models are used as the measurement model of the numerical tests and the MAGSAT data, respectively. The measurement model of Eq. (2) using the IGRF model is

$$h(\boldsymbol{x},t)=\sqrt{\left[B_r^2(r,\theta,\phi)+B_\theta^2(r,\theta,\phi)+B_\phi^2(r,\theta,\phi)\right]} \tag{4}$$

where the functions B_r, B_θ, and B_ϕ represent the down, east, and north components of the Earth's magnetic field vector at location (r,θ,ϕ). As the IGRF model is a function of the position vector in the International Terrestrial Reference Frame (ITRF), the state vector of the inertial frame has to be transformed to ITRF using the Greenwich apparent sidereal angle and the Earth's nutation and precession angles. These angles have been calculated by an analytical method for computational efficiency [17]. The UT1-UTC and polar motion are considered as a constant due to their relatively small daily variation, and have been set to the values at the epoch, i.e., 0.355491 for UT1-UTC (s), −0.32 for UTC-TAI (s), and (0.04328, 0.37783 in) for the polar motion. The measurement model error is modeled as a white Gaussian distribution with a different standard deviation from 10 to 100 nT, to determine how measurement noise affects the orbit determination results. An additional error worth noting is a bias in the sensor, if the bias is not calibrated properly before the filtering process. In this study, the effects of the bias are analyzed and the method of estimating the bias of each axis examined to eliminate errors caused by the bias.

C. Estimation Method: Unscented Kalman Filter

The most important feature of the UKF is computing the mean and the covariance of nonlinearly transformed variables from selected variables of so-called sigma points without the need for a linear approximation of the nonlinear function, as is done by the EKF [16]. The system and measurement equations are given by

$$\boldsymbol{x}_{k+1}=\boldsymbol{F}(\mathbf{x}_k,\boldsymbol{w}_k,t_k) \tag{5}$$

$$y_k=h(\boldsymbol{x}_k,t_k)+\eta_k \tag{6}$$

The state vector at t_k, $\boldsymbol{x}_k$, has dimension of $(n\times 1)$ with a covariance of $\boldsymbol{P}_k$ and y_k is the scalar measurement. In addition, $\boldsymbol{w}$ and η are the process noise vector $(q\times 1)$ and the measurement noise, each of which has a zero-mean Gaussian distribution with covariance of $\boldsymbol{Q}_k$ and $\boldsymbol{R}_k$, respectively. The specific number of the state vector and process noises, i.e., (n,q) is dependent on the dynamic model applied: (6,3) for Cases A–C, (7,4) for Cases D–E, and (8,5) for Case E with estimation of a single bias. The UKF prediction process starts with the selection of sigma points, which are the set of points around the reference point defined as the augmented state vector, $\boldsymbol{x}^a\{=[\boldsymbol{x}_k^T,\boldsymbol{w}_k^T(=\mathbf{0})]^T\}$, by adding and subtracting the square root of the scaled covariance matrix to/from the reference augmented state vector $(\boldsymbol{\chi}^a=\{\boldsymbol{x}^a,\boldsymbol{x}^a\pm[\sqrt{(L+\lambda)\boldsymbol{P}^a}]_i\},\ i=1,\ldots,L)$ [21]. The dimension of the augmented state L is $n+q$, and each sigma point consists of state $\boldsymbol{\chi}^x$ and process noise $\boldsymbol{\chi}^w$. The scaling parameter, $\lambda[\equiv\alpha^2(L+\kappa)-L]$ determines the extent of the sigma points along with the constant α which is set usually to a small positive value. The secondary scaling parameter κ is generally set to 3-L (see [9] for details). $[\sqrt{(L+\lambda)\boldsymbol{P}^a}]_i$ denotes ith column of the matrix square root of the augmented covariance $\boldsymbol{P}^a$. The total number of sigma points is $2L+1$. Each sigma point is propagated to the next measurement time (t_{k+1}) using the Eq. (5). The measurement $(\gamma_{k+1,i})$ at each propagated sigma point $(\boldsymbol{\chi}_{k+1,i})$ is also calculated using Eq. (6). Therefore, the computation time of the UKF depends on the dimension of the augmented state vector. In the current study, the augmented state vector is defined by adding only the process noise to the state vector because of the additive form of the measurement noise. This helps the computational speed as a result of a decrease in the number of sigma points. The predicted state and modeled measurement vector and their covariances (denoted by the upper bar) are calculated as a form of the weighted mean of the propagated sigma points $(\boldsymbol{\chi}_{k+1})$ and the measurement $(\boldsymbol{\gamma}_{k+1})$ through the nonlinear functions as follows.

$$\bar{\boldsymbol{x}}_{k+1}=\sum_{i=0}^{2L}W_i^{(m)}\boldsymbol{\chi}_{k+1,i},\qquad i=0,\ldots 2L \tag{7}$$

$$\bar{\boldsymbol{P}}_{k+1}=\sum_{i=0}^{2L}W_i^{(c)}(\boldsymbol{\chi}_{k+1,i}-\bar{\boldsymbol{x}}_{k+1})(\boldsymbol{\chi}_{k+1,i}-\bar{\boldsymbol{x}}_{k+1})^T \tag{8}$$

$$\bar{y}_{k+1}=\sum_{i=0}^{2L}W_i^{(m)}\gamma_{k+1,i} \tag{9}$$

$$\boldsymbol{P}^{y}_{k+1}=\sum_{i=0}^{2L}W_i^{(c)}(\gamma_{k+1,i}-\bar{y}_{k+1})(\gamma_{k+1,i}-\bar{y}_{k+1})^T+\boldsymbol{R}_{k+1} \tag{10}$$

The cross-correlation matrix $\boldsymbol{P}^{xy}$ of $\boldsymbol{x}$ and $\boldsymbol{y}$ is computed by

$$\boldsymbol{P}^{xy}_{k+1}=\sum_{i=0}^{2L}W_i^{(c)}(\boldsymbol{\chi}_{k+1,i}-\bar{\boldsymbol{x}}_{k+1})(\gamma_{k+1,i}-\bar{y}_{k+1}) \tag{11}$$

The weighing factors $(W_i^{(m)},W_i^{(c)})$ for the state and covariance are computed as follows:

$$W_i^{(m)}=\begin{cases}\frac{\lambda}{(L+\lambda)} & i=0\\ \frac{1}{2(L+\lambda)} & i=1,\ldots,2L\end{cases} \tag{12}$$

$$W_i^{(c)}=\begin{cases}\frac{\lambda}{(L+\lambda)}+1-\alpha^2+\beta & i=0\\ \frac{1}{2(L+\lambda)} & i=1,\ldots,2L\end{cases} \tag{13}$$

The third scaling parameter β plays a role in incorporating prior knowledge of the distribution of $\boldsymbol{x}$, and $\beta=2$ is known to be optimal for a Gaussian distribution [21]. The updated state and covariance (denoted by the upper hat) of the UKF applies the equations of the standard Kalman filter, namely [21]

$$\hat{\boldsymbol{x}}_{k+1}=\bar{\boldsymbol{x}}_{k+1}+\boldsymbol{K}_{k+1}(\tilde{y}_{k+1}-\bar{y}_{k+1}) \tag{14}$$

$$\hat{\boldsymbol{P}}_{k+1}=\bar{\boldsymbol{P}}_{k+1}-\boldsymbol{K}_{k+1}\boldsymbol{P}^{xy}_{k+1}\boldsymbol{K}^T_{k+1} \tag{15}$$

where $\tilde{y}_{k+1}$ is the observed measurement vector, and the gain matrix $\boldsymbol{K}_{k+1}$ is defined by

$$\boldsymbol{K}_{k+1}=\boldsymbol{P}^{xy}_{k+1}(\boldsymbol{P}^{y}_{k+1})^{-1} \tag{16}$$

The most important feature of the UKF is that it does not require linear approximation of the nonlinear dynamics and measurement equations. Consequently, the UKF in general estimates the state more accurately and robustly, and the algorithm might be implemented more easily compared to the EKF.

III. Numerical Results and Discussions

Numerical simulations have been conducted to analyze the performance of the UKF in the orbit determination problem and also to tune the dynamic model to the geomagnetic field measurements. The measurements were simulated for the low-Earth orbiting satellites with various orbital elements. All test cases covered 2 day arc data starting 1 January 2000, 12:00:00.0 (UTC). The three scaling parameters of the UKF, i.e., α, β, and κ are set to 1, 2, and 3-L, respectively, with L having a different value from case to case, i.e., 9 in Cases A–C, 11 in Cases D–E, and 13 for the single bias

Table 2 Position errors achieved through the unscented Kalman filter for various altitudes (highly inclined near-circular orbits)

	Average RSS (maximum error), km				
Study case	Alt. = 400 km	Alt. = 600 km	Alt. = 800 km	Alt. = 1000 km	Alt. = 1500 km
A	1.94 (2.83)	0.47 (1.11)	0.38 (1.06)	0.53 (1.58)	0.68 (1.60)
B	4.29 (6.02)	0.75 (2.07)	0.60 (2.07)	0.77 (1.91)	0.79 (1.97)
C	4.35 (5.67)	0.39 (0.99)	0.48 (1.10)	0.59 (1.82)	0.70 (1.62)
D	1.05 (2.82)	0.79 (2.16)	0.60 (2.06)	0.77 (1.91)	0.79 (1.97)
E	0.71 (1.79)	0.45 (1.12)	0.48 (1.10)	0.59 (1.82)	0.70 (1.62)

estimation case. However, in the current study the results are not affected by α at values between 0.001 and 1.

A. Effects of Dynamic Models

The orbit determination process was conducted for near-circular, highly inclined (98.3 deg) orbits of various altitudes from 400 to 1500 km. The other initial values (e, Ω, ω, and ν) of the true orbit are set to zero. The true orbits were calculated precisely by the HPOP module and were compared with the orbits obtained from all five dynamic model cases shown in Table 1. The measurement data set was generated including noise of 20 nT (1 σ) to the simulated magnetometer data using a data-sampling period of 30 s. Initial position errors of 500 km magnitude are assumed by setting 300 km for each component of the position vector. The initial covariance matrix $\boldsymbol{P}_0^x$ is diagonal with position, velocity, and B^* elements, which are set to $P_{\text{pos}} = (30\text{ km})^2$, $P_{\text{vel}} = (30\text{ m/s})^2$, and $P_{B^*} = (0.001)^2$. To find the appropriate initial covariance value, four different initial position errors (3, 30, 100, and 300 km) and four different initial covariances $(P_{\text{pos}}, P_{\text{vel}})$ were tested: $\{(1\text{ km})^2, (1\text{ m/s})^2\}$, $\{(10\text{ km})^2, (10\text{ m/s})^2\}$, $\{(30\text{ km})^2, (30\text{ m/s})^2\}$, and $\{(100\text{ km})^2, (100\text{ m/s})^2\}$ of position and velocity components, respectively. The results showed the filter is not sensitive to the initial covariance if the initial error is given less than 10 times of initial covariance (i.e., 10 σ_{pos}). Therefore, the initial covariance value of these tests is near a minimum value when the initial position error is about 300 km. The filter can diverge when the initial covariance is set to less than a tenth of the initial position error. This phenomenon occurred because the filter smugness which denotes too small covariance can cause the filter to ignore new measurements. Therefore, it may be concluded that the UKF is also sensitive to the initial covariance, similar to the EKF, and that larger initial covariance should be set when the initial position errors are larger than those of the current test cases. The covariance of $B^*(P_{B^*})$ is used only for Case D and Case E.

Table 2 summarizes the average root sum square (RSS) of the position errors as well as the maximum error for all the altitudes. The average RSS and the maximum error are calculated from nontransient state; that is, from 20 to 48 h of elapsed time in this study. A difference between the average RSS position error and the maximum error represents the amplitude of the fluctuating position errors. In most cases, the maximum position error is reduced from 500 km to below 5 km in the first 5 h. Cases D and E, which include atmospheric drag, yield relatively accurate results at an altitude of 400 km compared with the results from Cases B and C, as the maximum position error decreases to 2.82 and 1.79 km, respectively. Results from altitudes above 600 km show there are no significant differences between the ballistic coefficient estimate cases and the nonballistic coefficient estimate cases (between Cases B and D, and between Cases C and E). Sometimes, the ballistic estimate case at 600 km altitude shows marginally worse results than the nonballistic coefficient estimate case (within 1 σ, i.e., 0.3 km). This is because the geomagnetic field measurements do not have sufficient resolution at that altitude to estimate the ballistic coefficient precisely. When the geopotential coefficients are increased from 2×0 (J2 effect) to 4×4 for the geopotential perturbation calculation, both the average RSS and the maximum error are improved at all altitudes. At altitudes of 600 and 800 km, the results of Cases C and E, including the geopotential coefficients 4×4, show that the maximum position error decreases to one-half of that of Cases B and D (only J2 effect): i.e., from about 2 to 1 km. On the other hand, Case A is not very effective at improving the orbit determination results although this case includes more sophisticated acceleration terms than the other cases. At 400 km altitude, the results from Case A indicate that a precisely modeled dynamic model not including estimation of the ballistic coefficient can yield poorer position accuracy than coarsely modeled cases including the ballistic coefficient (i.e., Cases D and E). However, Case A includes atmospheric drag with the assumption of the constant ballistic coefficient with 20% error added to the value of the true model, because the ballistic coefficient can vary by as much as 20–80% due to a variety of reasons including altitude, solar activity, and attitude [22]. As an example, the evolutions of the position errors in Cases A–E at 400 km altitude are plotted in Fig. 1. In Fig. 1, the evolution of the covariance (σ_{pos}) in of Case E is added as a narrow black line and shows that the true estimation error is well matched with the estimated covariance matrix.

In this study, the estimate of the ballistic coefficient does not improve the achieved position errors at altitudes higher than 800 km. However, at an altitude of 400 km, the position error is reduced to 2.82 km in Case D from 6.02 km in Case B by estimation of the ballistic coefficient. In summary, it can be concluded that the dynamic model of Case E is the best suited to the majority of low-Earth orbits. Hence, the following tests are conducted using the dynamic model of Case E.

B. Effects of Orbit Types

A magnetometer-based orbit determination is based on the principle that the distribution of the geomagnetic field along the orbit has adequate resolution to identify the specific orbit. Therefore, the measured data range of the geomagnetic field along the orbit should be large enough to allow a precise orbit reconstruction. The range of the measured data is highly dependent on the type of orbit as the Earth's magnetic field resembles, in general, a field generated by a dipole magnet (i.e., a straight magnet with a north and south pole) located at the center of the Earth, with the axis of the dipole being offset from the axis of the Earth's rotation by approximately 11 deg.

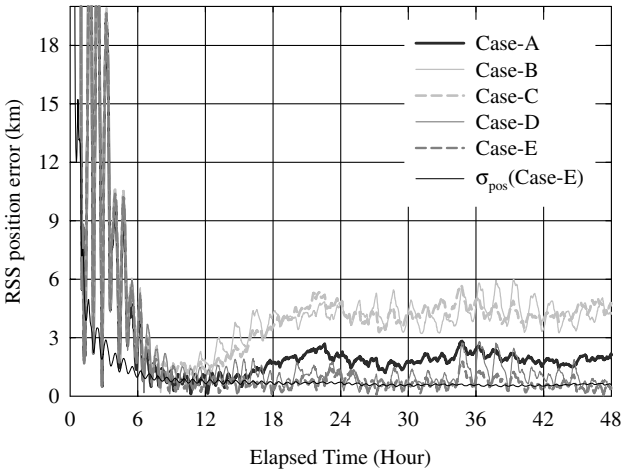

Fig. 1 Evolution of the RSS position errors of Cases A–E for the near-circular highly inclined orbit with 400 km altitude.

Table 3 Average RSS (maximum) errors, km, for the different eccentricities and inclinations; the other orbital elements (Ω, ω, and ν) are set to zero

Inclination	Eccentricity (perigee alt. = 400 km)	RSS, km	Max. Err., km	(Max–min) of measurements, nT
$i = 0$ deg	0.0000 (apogee alt. = 400 km)	4.02	7.33	12,438
	0.0287 (apogee alt. = 800 km)	2.59	8.60	15,566
	0.0623 (apogee alt. = 1300 km)	4.84	9.58	19,047
	0.1056 (apogee alt. = 2000 km)	5.78	8.02	22,630
$i = 30$ deg	0.0000	2.67	7.71	27,925
	0.0287	1.95	4.18	26,340
	0.0623	1.99	5.00	26,037
	0.1056	2.42	5.36	26,966
$i = 60$ deg	0.0000	1.18	3.48	35,233
	0.0287	0.79	2.56	34,057
	0.0623	0.99	2.45	34,133
	0.1056	1.48	3.31	34,800
$i = 90$ deg	0.0000	0.99	2.69	35,129
	0.0287	0.74	1.90	35,385
	0.0623	0.82	2.14	36,508
	0.1056	0.68	1.72	37,378

Hence, the orbital type is of crucial importance for the accuracy of a magnetometer-based orbit determination method. These properties can be seen from tests of how orbit accuracy is influenced by a range of the geomagnetic field as the eccentricity and inclination vary. The measurement and the true orbit are sampled at 30-s intervals using 20 nT (1 σ) for the magnetometer noise and the HPOP model for orbit propagation. The initial orbit of each orbit type and the corresponding results are summarized in Table 3. The eccentricity range is from zero to over 0.1, and the inclination range is from 0 to 90 deg. The dynamic model of Case E is used for all tests, and the initial position errors are assumed to be 300 km for each axis. The initial covariance matrix $\boldsymbol{P}_0^x$ is assumed to be a diagonal matrix with position, velocity, and B^* elements, set to $P_{\text{pos}} = (100\text{ km})^2$, $P_{\text{vel}} = (100\text{ m/ sec})^2$, and $P_{B^*} = (0.001)^2$. The results in Table 3 show that the achieved position accuracy is clearly not dependent on the eccentricity and is crucially dependent on the inclination of the orbit. For an equatorial orbit, the average RSS position error (excluding the transient state; first 30 h) is extended by 5 km, whereas for a polar orbit, the average RSS position error (excluding the transient state; first 20 h) is less than 1 km (see Fig. 2). This phenomenon is related significantly to the range of the measured geomagnetic data shown in the last column of Table 3: i.e., the difference between the minimum and maximum values of the geomagnetic measurements. Although the small variation in the measurements in an equatorial orbit causes the lower position accuracy and a slower converging speed than in the case of a highly inclined orbit, the variation in an equatorial orbit provides sufficient observability of the orbital states.

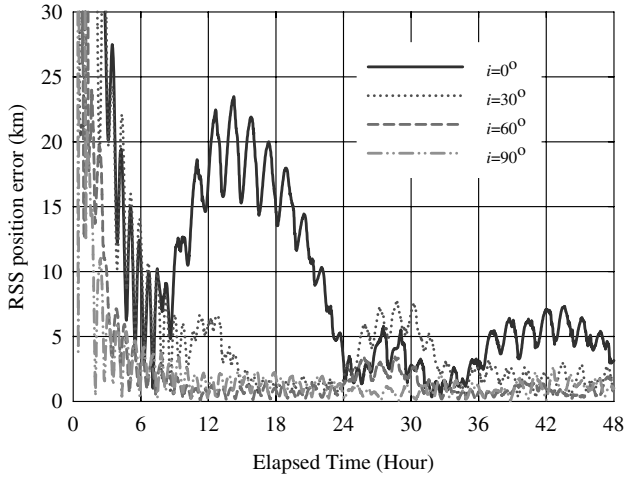

Fig. 2 Evolution of the RSS position errors for different orbital inclinations ($e = 0$).

C. Effects of Measurement Errors

To examine the effects of measurement noise on position accuracy, different levels of measurement noise are applied using the dynamic model of Case E. The measurement data are generated from the true orbit generated by the HPOP module with 600 km altitude, 98.3 deg inclination, and zero for the other orbital elements. Standard deviations of 10, 50, and 100 nT in each axis and biases of 10 and 50 nT in a single axis (x-axis) were assumed when the measurement data were generated artificially. The initial estimate position errors are assumed to be 100 km for each axis, and the initial covariance is applied to be the same as that of the subsection "Effects of Dynamic Models." The average RSS of the position errors and the maximum errors calculated, excluding the transient state (first 5 h), are summarized in Table 4. This table shows smaller Gaussian noise in the measurements led to better position accuracy. Even in the case with data noise of 100 nT, the average RSS position error is at a level of 1 km. However, even a small measurement bias can cause a considerable degradation of filter performance. By estimating the bias, the maximum position error is reduced from 19.6 to 2.0 km when a 50 nT bias is applied in a single axis. When a 10 nT bias is applied to all three axes, estimation of the biases reduced the maximum error from 3.41 to 1.32 km. In these tests, biases are modeled as a random walk, similar to the ballistic coefficient with process noise of 0.1 nT (1 σ). Figure 3 shows the evolution of position errors and the estimated bias for the cases, with and without estimation of bias as a state variable, in addition to position, velocity, and the inverse of the ballistic coefficient. This means that the bias estimation should be included, especially when the bias of the sensor is not calibrated properly. Note that the attitude of the satellite should be known for estimation of the biases.

D. Comparison with the Extended Kalman Filter

In this subsection, the performance of the UKF in the magnetometer-based orbit determination is compared with the results achieved through the EKF. Some conditions that allowed fair comparisons of the two filters should be noted. First, a Cartesian orbit representation has been selected for both the EKF and UKF filter which avoids singularities in the orbit representation and difficulties with sigma point handling in the UKF [4]. Second, the filter tuning, i.e., the selection of appropriate initial covariances and process and measurement noise, has been performed such that each filter is operated under adequate conditions, being achieved through slightly different tuning parameters.

The comparisons of the UKF with the EKF are conducted for various sampling periods, ranging from 10 to 40 s. The measurement data are artificially generated from the true orbit, which is calculated using the HPOP for the near-circular orbit at an altitude of 600 km, at an inclination of 98.3 deg, with the other elements set to zero. The equatorial orbit with a 40-s sampling interval is also compared to

Table 4 Average RSS and maximum error for different measurement noise and bias conditions

Noises	RSS, km	Max. Error, km
Gaussian noise: 10 nT	0.33	1.08
Gaussian noise: 50 nT	0.84	3.08
Gaussian noise 100 nT	1.35	4.33
Gaussian noise: 20 nT + bias; 10 nT in one axis	2.40	3.88
Gaussian noise: 20 nT + bias; 50 nt in one axis	11.96	19.62
Gauusian noise: 20 nT + bias; 10 nT in three axes	2.04	3.41
Gaussian noise: 20 nT + bias; 10 nT in one axis with bias estimation	0.48	1.72
Gaussian noise: 20 nT + bias; 50 nT in one axis with bias estimation	0.53	2.02
Gauusian noise: 20 nT + bias; 10 nT in three axes with bias estimation	0.60	1.32

evaluate differences in the decomposed position errors (i.e., radial, along-, and cross-track direction) in both filters. The 20 nT (1 σ) of measurement noise is applied to each magnetometer. The filter parameters (initial position errors, initial covariance, and measurement noise level) are set to the same parameters in both filters as follows:

$$\boldsymbol{r}_0 = \boldsymbol{r}_{\text{true}} + \begin{bmatrix} 10\text{ km} & 10\text{ km} & 10\text{ km} \end{bmatrix}^T, \qquad \boldsymbol{v}_0 = \boldsymbol{v}_{\text{true}} \qquad B_0^* = 0.01$$

$$\boldsymbol{P}_0^x = \text{diag}[(3\text{ km})^2, (3\text{ km})^2, (3\text{ km})^2, (3\times 10^{-3}\text{ km/s})^2,$$

$$(3\times 10^{-3}\text{ km/s})^2, (3\times 10^{-3}\text{ km/s})^2, (0.001)^2]$$

$$\sigma_{w1-w3} = 1\times 10^{-4}\text{ m/s}^2 \qquad \sigma_{w4} = 1\times 10^{-5}, \quad \text{and} \quad \sigma_\eta = 20\text{ nT}$$

However, the process noises for acceleration uncertainty are set to 1×10^{-4} m/s^2 in both filters, which is a bit higher than the tests in the previous sections (i.e., 1×10^{-5} m/s^2) to absorb the linearization error of the EKF longer sampling period. It is well known that the UKF is superior to the EKF when large initial estimate errors occur in many nonlinear estimation problems [10,11] as well as orbit determination problem [13,14]. Therefore, the initial position error is set to 10 km per each axis in these comparison tests. The dynamic model of Case E is used in both the filters. The results are summarized in Table 5 including the maximum errors of the decomposed position errors as well as the average RSS position error and the maximum error. The covariance evolution of the EKF is also well matched with the true estimation errors. For the 98.3 deg inclination case with a 20-s measurement interval, the true standard deviation of x-component during the last 5 h is 0.51 km and the average estimated σ_x is 0.49 km.

The results show that the position errors (the average RSS position error and the maximum error during the last 28 h) from the EKF were slightly better than the UKF in cases with a sampling interval of less than 20 s, whereas the UKF yields more accurate position estimation than the EKF in cases with a 40-s sampling interval. For the sampling period of 10 s, the maximum position error from the EKF is 0.72 km, whereas the maximum error increased to 3.53 km for the 40-s sampling interval. For the cases using the UKF, the difference in the maximum position error between the two sampling periods is just less than 1 km. These results indicate that the orbit determination problem is a fairly linear system in short sampling period, and that the UKF may be better than the EKF in a sampling interval over 40 s due to the system's nonlinearity. As can be seen in Table 5 and Fig. 4, in the EKF along-track error is dominant in an equatorial orbit, whereas in a near-polar orbit, cross-track error is dominant. On the other hand, along-track error is dominant in both near-polar and equatorial orbits in the UKF. The along-track component errors in both filters occur as a result of rapid changes in state variables in that direction. However, in the EKF, the cross-track errors are larger than the along-track in a near-polar orbit unlike the UKF. This discrepancy stems from the linearization process of the nonlinear measurement function, i.e., partial derivatives of $\boldsymbol{h}$ function with respect to the state variables. Namely, the accuracy of each component achieved through the EKF is influenced by the magnitude of the gradient of the geomagnetic field along each direction. When the magnitude of the gradients for the specific direction (component) is smaller than the other direction, the converging time in that direction is lengthy and the accuracy of that direction is also poorer than those of the other components. In the case of Fig. 4d, the average gradient along the longitudinal direction (cross-track) is 0.034 nT/rad, a value just one-fourth of the average gradient along the latitudinal direction (along-track). These disadvantages of the EKF also make strong in along-track error in an equatorial orbit. The inaccuracy of the cross-track error in the magnetometer-based orbit determination is also pointed out in [1].

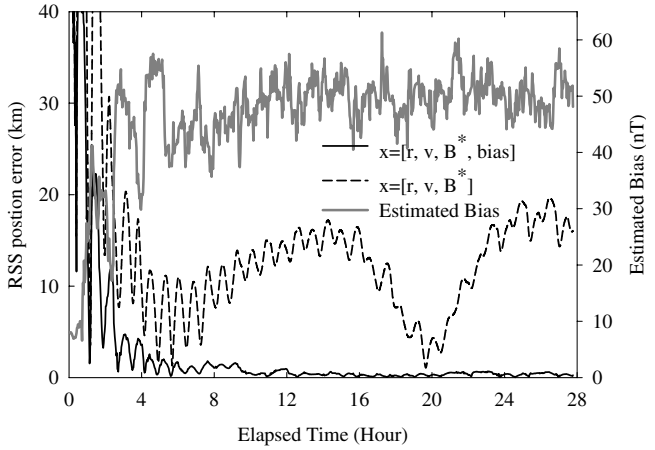

Fig. 3 Evolution of the RSS position errors for the case of with and without estimating bias [50 nT bias in x-axis as well as a Gaussian noise of 20 nT (1 σ) is applied in measurement data].

E. Results of the MAGSAT Case

The performance of the algorithm developed for the magnetometer-based orbit determination was tested using actual flight data obtained from the MAGSAT, which was launched in October 1979 to measure the magnetic field of near-Earth [23]. The perigee and apogee altitude of the MAGSAT is 351 and 578 km (hence eccentricity of 0.017), and the inclination is 96.8 deg. Although the MAGSAT measurement data are reasonably accurate, the data still have small jumps and periodic fluctuations despite calibration, and the standard deviation is approximately 30 nT. The MAGSAT's position, given along with the magnetometer data, is believed to have an accuracy of 60 m radially and 300 m horizontally [23]. Orbit determination through the EKF and the UKF was conducted using the dynamic model of Case E. Two sampling periods, 12 and 60 s, are applied, and the initial position and velocity errors are about 1000 km and 1 km/s, respectively. The evolutions of position errors shown in Fig. 5 were obtained using the MAGSAT's measurement data from 2 February 1980. At a sampling period of 60 s, the UKF (dashed line) shows better performance in both convergence rate and achieved position accuracy than the EKF (solid line). At a sampling period of 12 s (gray lines), although the convergence rate is similar in both filters (i.e., from 1000 km to less than 5 km in 12 h), the achieved position from the UKF is slightly more accurate than the EKF. The maximum errors of the UKF remained around 2 km after 1 day with 10-s sampling periods, and even at 60-s sampling interval the maximum errors is not greater than 3 km. The maximum errors of the EKF keep about 4 km only in the 12-s sampling period. The UKF results are also better than the results of [1] in both convergence rate and accuracy, which used the same measurement data and the square root information filter. In [1], it took about 24 h to decrease the

Table 5 Position errors achieved through the extended and unscented Kalman filter for various sampling periods (a near-circular orbit with 600 km altitude)

Sampling period/inclination	EKF, km		UKF, km	
	Average RSS (max. error)	max. errors of radial/along/cross	Average RSS (max. error)	Max. errors of radial/along/cross
10-s/98.3 deg	0.28 (0.72)	0.11/0.72/0.38	0.36 (1.11)	0.16/1.11/0.40
20-s/98.3 deg	0.38 (1.28)	0.19/0.93/1.23	0.43 (1.47)	0.22/1.42/0.34
40-s/98.3 deg	1.16 (3.53)	0.56/2.91/3.53	0.65 (1.89)	0.28/1.86/0.61
40-s/0.0 deg	2.58 (4.97)	0.10/4.48/0.21	1.33 (3.70)	0.23/3.70/0.44

position error of the MAGSAT from 1000 to 8 km, and the achieved position accuracy ranged from 4 to 8 km. The UKF results are comparable to the results of Jung and Psiaki [7] who showed that the position error of the MAGSAT could be improved from 7 to 3 km through the batch filter and the magnetic field model correction using a two-day data set. Incidentally, the computation time of the UKF is generally three times longer than the EKF, whereas the UKF with a 60-s interval case is comparable to the EKF with a 12-s intervals (i.e., about one-half of the computing time of the EKF with a 12-s interval).

IV. Conclusions

A magnetometer-based orbit determination algorithm using the unscented Kalman filter was developed and the properties of the method analyzed using extensive numerical tests for various orbital types, several measurement sampling periods, and various levels of measurement errors. The best suitable dynamic model for the majority of low-Earth orbits is chosen from the tests using various combinations of accelerations and includes the geopotential coefficient up to 4×4 and estimates of the ballistic coefficient as a state variable. In particular, the ballistic coefficient estimate should be included at altitudes lower than 400 km. The UKF shows that the position can be determined with a maximum error of less than 2 km for the low-Earth near-polar orbit. However, the error increases to about 9 km as the orbital inclination becomes closer to zero, due to the low variation of the equatorial geomagnetic field. The tests for various levels of measurement errors show that Gaussian noise up to 100 nT ($1\ \sigma$) is effectively removed. Even though a single bias causes critical degradation of the performance, this degradation can be recovered by estimating the biases as state variables.

The results of the performance comparisons between the UKF and the extended Kalman filter indicate that the UKF has a priority in the state estimation of the nonlinear satellite orbit system only for longer sampling periods. Namely, the determined position accuracy by the EKF is more dependent on the sampling period due to its linearization error than the UKF. Also, the radial, along-, and cross-track components of the position error are influenced by linearization of the measurement model when the EKF is used. Actual flight data of the MAGSAT satellite have been applied within a UKF to achieve convergence in 12 h from an initial position error of 1000 km and reaching a final position error of about 2 km. The algorithm in this paper can be used for various small explorer missions that require position accuracies of several kilometers.

Acknowledgments

This work has been supported by the Korea Institute of Science and Technology Evaluation and Planning as the program for Core

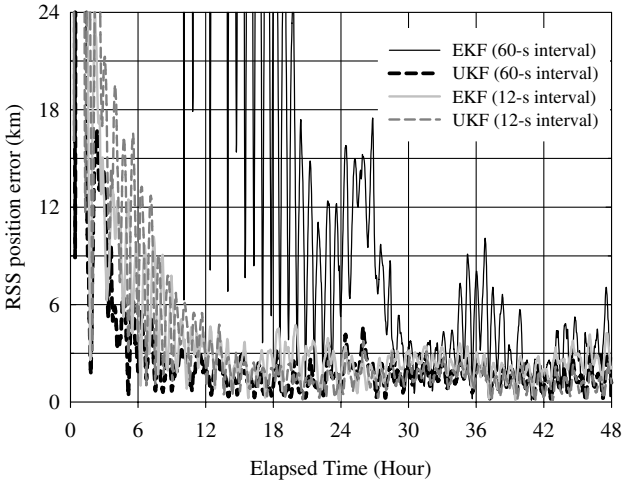

Fig. 5 Evolution of the RSS position error of the MAGSAT for 12 and 60-s measurement intervals.

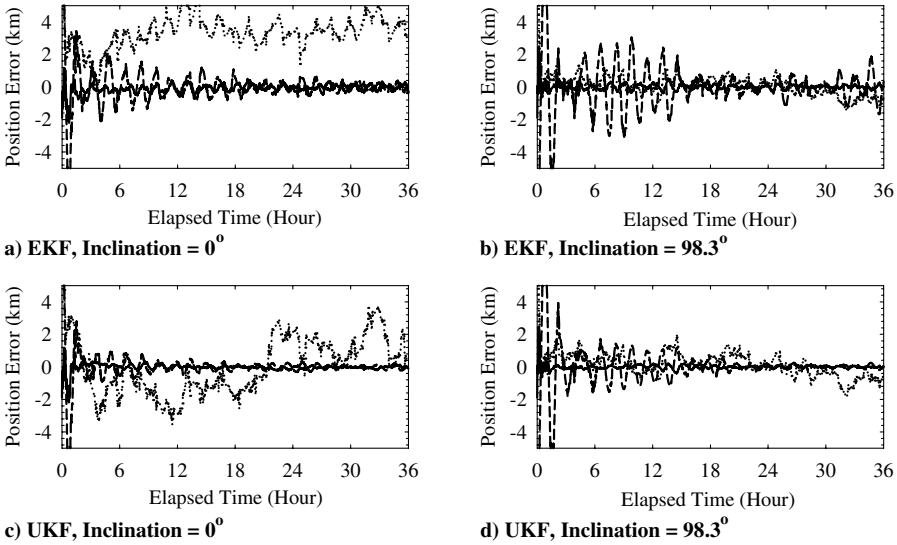

Fig. 4 Evolution of three components of position errors achieved through the UKF and EKF for the inclination of 0 and 98.3 deg at 40-s sampling interval (solid—radial, dotted—along-track, dash—cross-track).

Space Base-Technology. Data from the MAGSAT spacecraft were provided by the National Space Science Data Center in USA.

References

[1] Psiaki, M. L., Huang, L., and Fox, S. M., "Ground Tests of Magnetometer Based Autonomous Navigation (MAGNAV) for Low Earth Orbiting Spacecraft," *Journal of Guidance, Control, and Dynamics*, Vol. 16, No. 1, 1993, pp. 206–214.

[2] Shorshi, G., and Bar-Itzhack, I. Y., "Satellite Autonomous Navigation Based on Magnetic Field Measurements," *Journal of Guidance, Control, and Dynamics*, Vol. 18, No. 4, 1995, pp. 843–850.

[3] Wiegand, M., "Autonomous Satellite Navigation via Kalman Filtering of Magnetometer Data," *Acta Astronautica*, Vol. 38, Nos. 4–8, 1996, pp. 395–403.

[4] Deutschmann, J. K., and Bar-Itzhack, I. Y., "Evaluation of Attitude and Orbit Estimation Using Actual Earth Magnetic Field Data," *Journal of Guidance, Control, and Dynamics*, Vol. 24, No. 3, 2001, pp. 616–623.

[5] Cheon, Y-J., "Unscented Filtering Approach to Magnetometer-Only Orbit Determination," ICCAS Paper 2003-21, Oct. 2003.

[6] Psiaki, M. L., "Autonomous Orbit and Magnetic Field Determination Using Magnetometer and Star Sensor Data," *Journal of Guidance, Control, and Dynamics*, Vol. 18, No. 3, 1995, pp. 584–592.

[7] Jung, H., and Psiaki, M. L., "Tests of Magnetometer/Sun-Sensor Orbit Determination Using Flight Data," *Journal of Guidance, Control, and Dynamics*, Vol. 25, No. 3, 2002, pp. 582–590.

[8] Lowes, F. J., "An Estimate of the Errors of the IGRF/DGRF Field 1945-2000," *Earth, Planets and Space*, Vol. 53, No. 12, 2000, pp. 1207–1211.

[9] Julier, S. J., Uhlmann, J. K., and Durrant-Whyte, H. F., "A New Approach for Filtering Nonlinear Systems," *Proceedings of the American Control Conference*, American Automatic Control Council, Evanston, IL, 1995, pp. 1628–1632.

[10] Farina, A., Ristic, B., and Benvenuti, D., "Tracking a Ballistic Target: Comparison of Several Nonlinear Filters," *IEEE Transaction on Aerospace and Electronics*, Vol. 38, No. 3, 2002, pp. 854–867.

[11] Crassidis, J. L., and Markley, F. L., "Unscented Filtering for Spacecraft Attitude Estimation," *Journal of Guidance, Control, and Dynamics*, Vol. 26, No. 4, 2003, pp. 536–542.

[12] Ma, G-F., and Jiang, X-Y., "Unscented Kalman Filter for Spacecraft Attitude Estimation and Calibration Using Magnetometer Measurements," *IEEE Proceedings of the Fourth International Conference on Machine Learning and Cybernetics*, IEEE Publications, Piscataway, NJ, Aug. 2005, pp. 506–511.

[13] Lee, D.-J., and Alfriend, K. T., "Precise Real-Time Satellite Orbit Estimation Using the Unscented Kalman Filter," AAS Paper 03-230, Feb. 2003; also in *Advances in the Astronautical Sciences*, Vol. 114, Pt. 3, pp. 853–1872.

[14] Lee, D.-J., and Alfriend, K. T., "Sigma Point Filters For Efficient Orbit Estimation," AAS Paper 03-525, Aug. 2003; also in *Advances in the Astronautical Sciences*, Vol. 116, Pt. 1, pp. 349–372.

[15] Lee, D.-J., and Alfriend, K. T., "Adaptive Sigma Point Filtering For State and Parameter Estimation," AIAA Paper 2004-5101, Aug. 2004.

[16] Brown, R. G., and Hwang, P. Y. C., *Introduction to Random Signals and Applied Kalman Filtering*, 3rd ed., Wiley, New York, 1997, pp. 260–264.

[17] Montenbruck, O., and Gill, E., *Satellite Orbits: Models, Methods, and Applications*, Springer–Verlag, Berlin, 2000, Chaps. 3, 5.

[18] STK, Satellite Tool Kit Software, Ver. 4.0, Analytical Graphics, Inc., Malvern, PA, 1998.

[19] Yoon, J. C., Lee, K. H., Lee, B. S., Kim, B. Y., Choi, K. H., Chang, Y. K., Chun, Y. S., and Ra, S. W., "Geostationary Orbit Determination for Time Synchronization Using Analytical Dynamic Models," *IEEE Transactions on Aerospace and Electronic Systems*, Vol. 40, No. 4, 2004, pp. 1132–1146.

[20] International Association of Geomagnetism and Aeronomy (IAGA) Division V, Working Group VMOD, "The 10th-Generation International Geomagnetic Reference Field," *Geophysical Journal International*, Vol. 161, No. 3, 2005, pp. 561–565.

[21] Wan, E., and van der Merwe, R., *Kalman Filtering and Neural Networks*, edited by S. Haykin, Wiley, New York, 2001, Chap. 7.

[22] Bowman, B. R., "True Satellite Ballistic Coefficient Determination for HASDM," AIAA Paper 2002-4887, 2002.

[23] Langel, R., Berbert, J., Jennings, T., and Horner, R., "Magsat Data Processing: A Report for Investigators," NASA TM-82160, Nov. 1981.

C. McLaughlin
Associate Editor